Swelling of Steel Film by Hydrogen Absorption at Cathodic Potential in Electrolyte

Debi Garai, Ilaria Carlomagno, Vladyslav Solokha, Axel Wilson, Carlo Meneghini, Christian Morawe, Vadim Murzin, Ajay Gupta, Jörg Zegenhagen

physica status solidi pss b
www.pss-b.com

Swelling of Steel Film by Hydrogen Absorption at Cathodic Potential in Electrolyte

*Debi Garai, Ilaria Carlomagno, Vladyslav Solokha, Axel Wilson, Carlo Meneghini, Christian Morawe, Vadim Murzin, Ajay Gupta, and Jörg Zegenhagen**

An ≈4 nm FeCrNi film, deposited on a Ru/B_4C multilayer (ML), is used to study cathodic hydrogen charging in electrolyte. A thin film on a ML allows obtaining precise quantitative information on surface metal composition and oxidation state using the X-ray standing wave technique combined with near-edge X-ray absorption spectroscopy. The metal composition is found being close to the composition of stainless steel (SS) 304, and, as for bulk steel, the outer 2 nm passive layer, consisting of oxidized iron and chromium, is depleted of nickel. Overall, it is found that the film represented a useful replica of the surface of bulk steel. Following exposure to 0.1 M KCl electrolyte at −0.6 V versus Ag/AgCl, 11.3 (±3)% swelling of the film by hydrogen absorption is observed. The estimated absorbed amount is exceeding reported bulk absorption under similar conditions by more than an order of magnitude. Strong hydrogen absorption appears to be enabled by the 2D character of the thin film, i.e., a significantly lower associated strain energy compared with bulk absorption. The strong surface swelling is suggested to be related to the lowering of the pitting corrosion resistance of SS surfaces reported following hydrogen exposure.

1. Introduction

Metals and metallic alloys in electrolyte such as sea water suffer from galvanic corrosion caused by a gradient of the electrochemical potential between cathodic and anodic regions.[1] In case of composite materials or alloys, such gradients arise also locally, even on the microscopic scale, because of the different nobilities, i.e., electrochemical potential of the contained elements/materials (see e.g., the study by Örnek et al.[2]). Exposed to electrolyte, local variations in nobility, i.e., variations in the electrochemical potentials, cause local potential differences, giving rise to local cathodic and anodic reactions and thus localized corrosion processes.[3]

Corrosion is typically associated with the anodic part of the reaction because of the associated oxidation and/or removal of material. However, the cathodic reaction can have a major influence on the corrosion process. In particular, the destructive effect of hydrogen absorption as a consequence of the cathodic hydrogen evolution reaction is well known.[4–6]

The total annual cost due to corrosion is substantial, exceeding 3% of global GDP.[7] Galvanic corrosion is particularly important because most metals of practical use are alloys. Steel, a most widely used construction material, is an alloy, depending on its application, composed of different metallic (and some nonmetallic) components with different nobilities. Many applications require steels that provide a high degree of corrosion resistance in harsh environments. For stainless steel (SS), this is facilitated by a rather thin, oxidized, passive surface region of just a couple of nanometer thickness.[8–11] Its specific properties protect the surface of the alloy from corrosion attack.[12,13] Unfortunately, the thus-achieved protection is not perfect. SS suffers in particular from a form of corrosion,

D. Garai, V. Solokha, Dr. A. Wilson, Dr. J. Zegenhagen
Diamond Light Source Ltd.
Harwell Science and Innovation Campus
Didcot, Oxfordshire OX11 0DE, UK
E-mail: jorg.zegenhagen@diamond.ac.uk

D. Garai, Dr. A. Gupta
Amity Centre for Spintronic Materials
Amity University
Noida 201313, Uttar Pradesh, India

The ORCID identification number(s) for the author(s) of this article can be found under https://doi.org/10.1002/pssb.202000055.

DOI: 10.1002/pssb.202000055

D. Garai
Amity Institute of Applied Sciences
Amity University
Noida 201313, Uttar Pradesh, India

Dr. I. Carlomagno, Prof. C. Meneghini
Dipartimento di Scienze
Universitá Roma Tre
Via della Vasca Navale 84, 00146 Rome, Italy

V. Solokha
Johannes Kepler University Linz
Altenberger Straße 69, 4040 Linz, Austria

Dr. C. Morawe
ESRF – The European Synchrotron
38043 Grenoble, France

Dr. V. Murzin
University Wuppertal
Gaußstraße 20, 42119 Wuppertal, Germany

called pitting,[3,14–17] which starts locally, on a small scale but eventually can become very destructive. The conditions and processes that initiate, govern, and/or influence the onset of corrosion, in particular, the destruction of the passive layer are subject of intense research. Investigating the microscopic root cause of the process requires techniques, being able to analyze surface/interface structure and chemistry on the atomic scale.

For gaining more information on surface processes upon galvanic corrosion, a combination of state-of-the-art X-ray spectroscopic techniques namely X-ray absorption near-edge structure (XANES),[18] and X-ray standing waves (XSW)[19–21] is used here. To trace structural and compositional changes down to the atomic level, an about 4 nm-thick iron–chrome–nickel film is used as the model of the crucial surface region of SS. A multilayer (ML) serves as the substrate, allowing using XSW measurements under Bragg's diffraction condition. In this way, the detailed depth profile of chromium, iron, and nickel is obtained. XANES is sensitive to the local environment and oxidation state of the absorbing atom. Performed under XSW excitation, XANES reveals the oxidation states of Cr, Fe, and Ni depth-selectively in the surface region. In this way, we resolved depth-selectively the composition of the film and changes following electrolyte exposure. Hydrogen absorption at cathodic potential caused major swelling of the film, which most probably was accompanied by disruption of the film.

Hydrogen absorption and destructive expansion of steel is well known. As mentioned earlier, it may happen or be enhanced locally, on the microscopic scale, driven by gradients in the electrochemical potential, resulting from local inhomogeneities in steel surface composition.[22–25] These are—whether they originate from material composition variations, impurities, and specific features from production or processing—generally understood to be the root cause for pitting corrosion.[3,16,26,27] The findings presented here shed new light on reports that hydrogen loading decreases the resistance of SS to pitting corrosion,[3,16,27–30] finally leading to embrittlement.[4–6]

2. X-Ray Standing Wave Analysis

An XSW is created during Bragg reflection. Its planes move inward by 1.85 nm, i.e., by half the d-spacing of the ML[20,31,32] (**Figure 1**a) when crossing the range of reflection. The XSW maxima move inward from a "position" defined as $P = 0.5$ via $P = 0.25$ to $P = 0$, and the mimima are moving from $P = 1$ via 0.75 to $P = 0.5$. The "position" P corresponds to a real-space position z (in the following associated with the film thickness) normalized to the wavefield spacing, which is identical to the ML "lattice spacing" d_{ML}, i.e., $P = z/d_{\mathrm{ML}}$. As the XSW is periodic, P is only defined modulo n (integer n) and, e.g., $P = 0$ and $P = 1$ are equivalent.

Due to the XSW movement, the emission profile of atoms located on the surface of the ML is modulated, as it is clearly visible for the K-fluorescence intensity of Cr, Fe, and Ni, as shown in Figure 1b. Such emission profiles have the generic form[31]

$$Y(E_\gamma) = I(E_\gamma)/I_0 = 1 + R(E_\gamma) + 2\sqrt{R(E_\gamma)}F_c \cos[\nu(E_\gamma) - 2\pi P_c] \tag{1}$$

In this case, $Y(E_\gamma)$ is the normalized X-ray fluorescence yield of Cr, Fe, or Ni, recorded when traversing the Bragg reflection. The intensity $I(E_\gamma)$ is normalized by the corresponding intensity I_0 measured far outside the range of Bragg reflection, i.e., for reflectivity $R(E_\gamma) = 0$.[31] The phase difference $\nu(E_\gamma)$ between incident and reflected waves is calculated with the knowledge of E_γ, the Bragg angle, and the structure of the ML (see the studies by Bedzyk and Libera[32] and Supporting Information). The parameter P_c called coherent position describes a "mean" position $\langle z_m \rangle$ of the distribution, here of the metal component (m = Cr, Fe, or Ni) normal to the reflection planes in fractions of the spacing of the XSW, i.e., $\langle z_m \rangle = d_{\mathrm{ML}} \cdot P_c \,(\mathrm{mod}\, n)$, and the parameter F_c (coherent fraction) describes the width of the

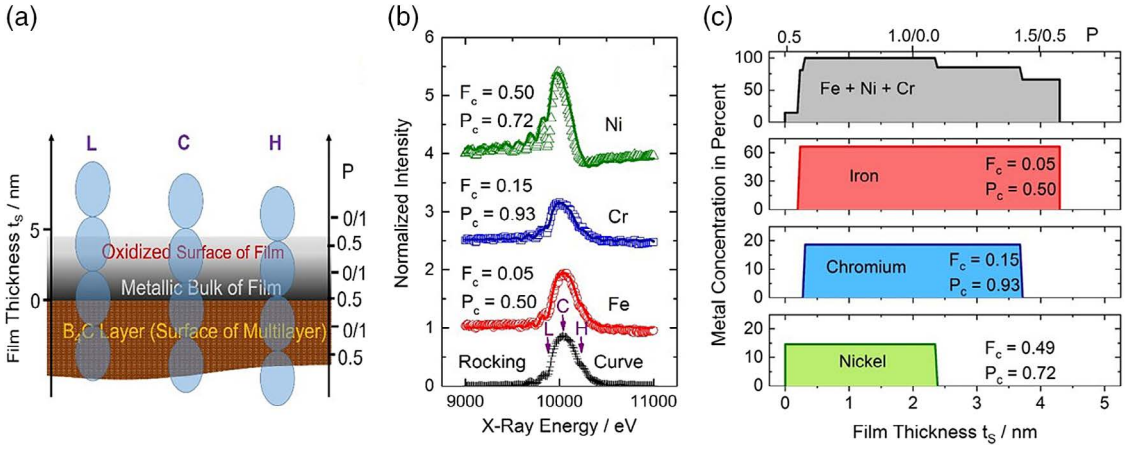

Figure 1. XSW analysis of FeCrNi film on RuB4C ML. a) Schematic of the thin film on the ML, indicating three positions of the X-ray standing wave for the low-energy (L), center (C), and the high-energy (H) side of the rocking curve, the three conditions selected for the XANES measurements. Traversing the rocking curve, the XSW maxima move inward by half the wavefield spacing d_{ML} from $P = 0.5$ via 0.25 to $P = 0/1$ and the mimima move from $P = 0/1$ via 0.75 to $P = 0.5$. Because of the periodicity of the XSW, P values are defined on a scale 0–1, modulo n, with $P = 0$ and $P = 1$, thus being equivalent. b) Result of the XSW measurement for the pristine film (symbols) and fits to the data (lines). The curves for Cr and Ni are vertically shifted for clarity. c) Best fit square box models of the distribution of Ni, Cr, and Fe in the film. The experimental coherent positions P_c and fractions F_c are very well reproduced. Only the width of the distribution of Fe extends beyond the wavefield spacing $d_{\mathrm{ML}} = 3.91$ nm.

distribution around this mean position[20,31] (see Supporting Information for more details). Both parameters are defined on a scale from 0 to 1, with $F_c = 1$ representing a delta-function-like sharp distribution and $F_c = 0$ describing a uniform distribution over the whole range of the wavefield spacing d_{ML}. Mathematically and more precisely, F_c and P_c of Ni, Cr, and Fe represent the amplitude and phase, respectively, of the coefficient H of the Fourier decomposition of the real-space distribution of the corresponding element, with $H = 1/d_{ML}$. Because of the periodic nature of the XSW, P_c values define real distances only modulo XSW period, here the d-spacing d_{ML} of the ML. Distances beyond d_{ML} cannot be determined without using additional information.

3. Results and Discussion

3.1. Pristine Film

The results of the XSW measurements for the pristine steel film are shown in Figure 1b. The yield curves of Cr, Fe, and Ni reveal clear differences, which means that the depth distribution of Cr, Fe, and Ni is not the same in the film. Equation (1) is fitted to each yield curve by varying F_c and position P_c. The results of best fits are shown in Figure 1b and **Table 1**. Both, F_c and P_c are significantly different for all three metals, meaning that both, the center of gravity and the width of the distributions, are different for all three metals. Judging by the coherent fractions F_c, Ni exhibits the narrowest and Fe the widest distribution. The coherent position P_c of Fe is the smallest, smaller than that for Ni, the coherent position of which in turn is smaller than that for Cr. However, the conclusion that Fe would be concentrated below Ni and Cr is premature.

Just by one XSW measurement, i.e., with one Fourier component for each of the metals, finer details of their distribution cannot be resolved. However, using a simple square box-like distribution, assuming constant concentration of each metal over a certain depth, the measured coherent fractions and positions can be reproduced and characteristic differences in the metal distribution can be resolved. Calculating the Fourier coefficients of a square box is a textbook problem. Assuming a square box profile, the experimental coherent positions mark the centers of the box profiles, i.e., $P_c = (P_2 + P_1)/2$, where P_2 and P_1 are the two boundaries of the box. The width of the box $\Delta P = P_2 - P_1$ is determined by the coherent fraction $F_c = 1/(\Delta P \cdot \pi)\sin(2\pi \cdot \frac{\Delta P}{2})$ (see Supporting Information for more details). Thus, to obtain the boundaries, ΔP is varied until the correspondingly calculated F_c best agrees with the experimental F_c.

The distribution of Fe extends beyond one XSW period, which is the reason for the coherent position, the seeming "mean position," being smaller than that for Cr and Ni. When the width ΔP of the box profile distribution ranging from P_1 to P_2 increases, the coherent position increases, given by $P_c = P_1 + \Delta P/2$. Once ΔP approaches 1.0, the width approaches the spacing d_{ML} of the XSW, the coherent position approaches $P_c = P_1 + 0.5$, accompanied by the coherent fraction going to zero. With ΔP increasing beyond 1.0, the coherent fraction increases again. However, the coherent position undergoes a phase jump. It increases further but starting again from P_1 according to $P_c = P_1 + \frac{\Delta P - 1}{2}$ (see the Supporting Information for more details).

Coherent fractions and positions for the three best-fitting square box profiles are shown in Table 1 and the corresponding boundaries P_1 and P_2 of the boxes are shown in **Table 2**. With P values translated into real-space distances/thicknesses, the resultant profiles are shown in Figure 1c. The experimental F_c and P_c values are very well reproduced. Using the metal concentration ratios of Fe/Cr = 4.3 and Fe/Ni = 9.0, as determined by X-ray fluorescence analysis, the concentrations are scaled and the total atomic concentrations of the metals as functions of film thickness t_s are calculated and shown in the upper panel of Figure 1c.

XSW analysis reveals clearly that ≈0.5 and ≈2 nm of the surface region is depleted of Cr and Ni, respectively. This is rather similar to the metal distribution in the surface of bulk SS 304[12,23,33] and in agreement with reports[8,12,23] that the ≈2 nm passive film on bulk steel is nickel free. According to the XSW derived model, the total thickness of the film is ≈4.5 nm, in good agreement with the X-ray reflectivity (XRR) data, but the metal density of the top 2 nm is reduced due to surface oxidation, as shown by the XSW/XANES measurements discussed in the following paragraphs. Overall, the deduced composition of the film is comparable with the surface composition of bulk SS304.[8,12,23,33]

XANES measurements, to be published in a forthcoming report,[34] revealed that about 80%, 70%, and 20% of Cr, Fe, and Ni, respectively, in the film were oxidized. To investigate

Table 1. Coherent fraction F_c and position P_c for Cr, Fe, and Ni obtained by fitting Equation (1) to the XSW data for the pristine and KCl exposed film and corresponding values calculated for a simple square box model.

Metal component		Pristine		After exposure to KCl	
		F_c	P_c	F_c	P_c
Fe	Exp. results	0.05 ± 0.03	0.50 ± 0.03	0.13 ± 0.04	0.62 ± 0.03
	Box model	0.05	0.50	0.17	0.59
Cr	Exp. results	0.15 ± 0.04	0.93 ± 0.03	0.10 ± 0.04	0.00 ± 0.03
	Box model	0.15	0.93	0.10	1.00
Ni	Exp. results	0.50 ± 0.05	0.72 ± 0.03	0.45 ± 0.05	0.79 ± 0.03
	Box model	0.49	0.72	0.45	0.79

Table 2. Boundaries P_1 and P_2 as well as widths $\Delta P = P_2 - P_1$ of metal distributions determined from experimental F_c and P_c based on square box model. Expansion factors e_F and e_P are calculated based on the experimental F_c only (e_F) as well as considering P_c (e_P).

					Expansion e [%]	
		P_1	P_2	ΔP	e_F	e_P
Pristine	Fe	0.48	1.52	1.04		
	Cr	0.5	1.36	0.86		
	Ni	0.42	1.02	0.6		
H-exposed	Fe	0.58	1.74	1.16	11.5	15.4
	Cr	0.55	1.45	0.9	4.7	8
	Ni	0.475	1.105	0.63	5.0	23

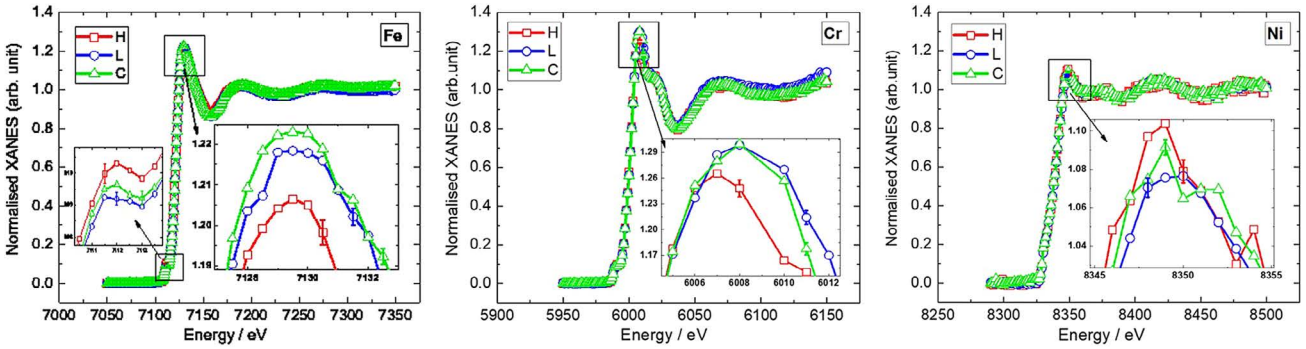

Figure 2. XANES spectra of Fe, Cr, and Ni for the pristine film. Passing the Bragg reflection curve from low-energy side (L) via center (C) to the high-energy side (H), maximum XSW intensity moves from the oxidized surface region into the bulk of the film (Figure 1a). Clearly shown in the insets, oxidation-related features in the Fe and Cr XANES decreased at H. The XANES spectrum of Ni, located ≥2 nm below the surface, reveals mostly metallic character and does not change significantly with the XSW movement.

the oxidation status of the metals depth-selectively, XANES measurements were carried out under XSW excitation, enhancing the X-ray intensity in three distinct regions in the steel film[35] (Figure 1a). Such measurements require adjusting the angle of incidence when changing the energy, such that XSW does not move during the XANES scan.

The position of XSW is encoded in the rocking curve (Figure 1a). Passing the range of Bragg reflection, XSW moves inward by $\frac{d_{ML}}{2}$.[21,31] The three XSW positions in the steel film chosen for XSW/XANES measurements are schematically shown by the three schemes of XSW in Figure 1a. They correspond to a reflectivity of 50% on the left slope (L = low-energy side), at the maximum (C = center), and at a reflectivity of 50% on the right slope (H = high-energy side) of the rocking curve (Figure 1b).

XANES spectra for Cr, Fe, and Ni acquired under these three conditions are shown in **Figure 2**. At the low-energy side (L) and at maximum (C), the dominant weight of X-ray intensity in the film is mostly located in its upper half, the surface region, whereas at the high-energy side, the maximum weight of intensity is located deeper in the film (Figure 1a). This is reflected in the Cr and Fe XANES spectra. The sharp XANES peak closest to the *K*-edge is characteristic of the oxidized metal states (Supporting Information). For Cr and Fe, the peak is most pronounced at L and C and less so at the high-energy side H of the rocking curve. This clearly shows that Cr and Fe are oxidized in the surface region and exhibit a more metallic character deeper below. The XANES spectrum of nickel, located deeper, close to the B_4C interface, shows a mostly metallic character, and the shape hardly changes with the XSW movement. The XSW/XANES measurements confirm that the composition of the steel film resembles the surface composition of bulk SS304.[8,12,23,33]

3.2. Electrolyte Exposed Film

Under control of a potentiostat, the film was exposed for 30, 120, and finally 480 s to 0.1 M KCl electrolyte at −0.6 V in a standard three-electrode electrochemical cell with a silver/silver-chloride (Ag/AgCl) reference and a Pt counter electrode.[34] The current recorded during the final 480 s exposure, resulting in a charge transfer of 0.030 A s cm^{-2}, is shown in **Figure 3**a. The total transferred cathodic charge of all three exposures was 0.038 A s cm^{-2}, corresponding to a total electron transfer of $2.4 \times 10^{17} e_0$ cm^{-2}.

The result of the XSW measurement, conducted ex situ immediately after the last cathodic electrolyte exposure, is shown in **Figure 4**a and F_c and P_c values are shown in Table 1. Coherent fractions F_c and coherent positions P_c changed significantly compared with the results for the pristine sample. The coherent positions of all three metals increased and the coherent fraction of Ni and Cr decreased, which can only be explained by an increase in the thickness for Ni and Cr. The coherent position for Fe increased almost twice as much as for Ni and Cr, whereas the coherent fraction also increased. In fact, the increase in the coherent fraction of Fe is also explained by an increase in the Fe thickness. The reason being that the width of the intrinsic Fe distribution was already slightly beyond the width of the

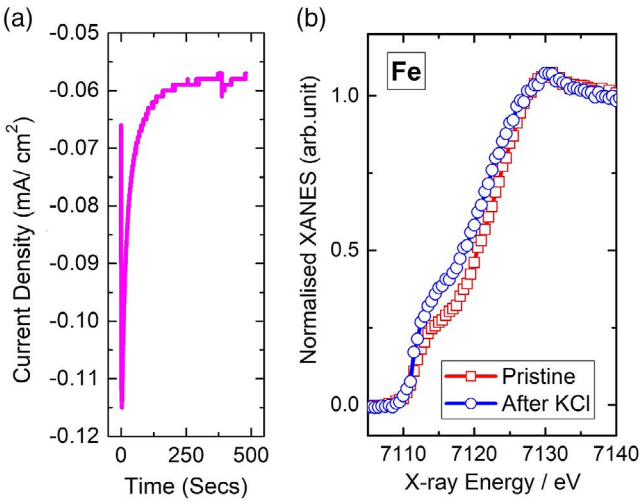

Figure 3. Exposure of steel film to 0.1 M KCl at $-0.6\ V_{Ag/AgCl}$. a) Current recorded for 480 s, exposure of 4 nm film and b) Fe K-edge XANES spectrum of a 6.5 nm film recorded before and after exposure. Increase in the pre-edge feature indicates the reduction of Fe oxide (Figure 2 and Supporting Information).

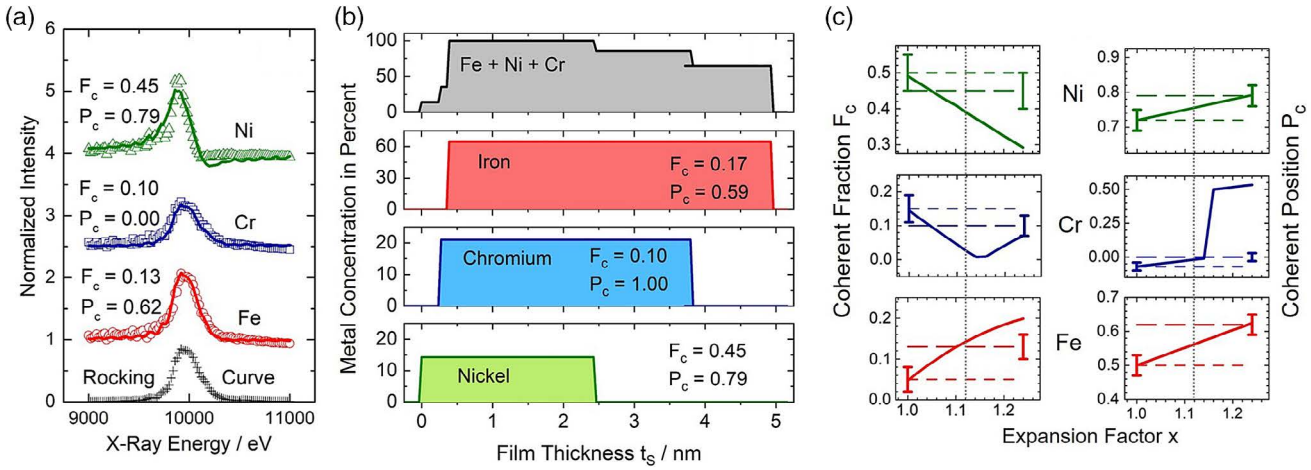

Figure 4. a) XSW results after exposure to KCl electrolyte at −0.6 V. Symbols are data and lines are fits to the data using Equation (1). b) Metal distribution with constant density profile best reproducing the experimental results. Note that the XSW results $P_c = 0$ and $P_c = 1$ are equivalent. c) Experimental and calculated coherent fractions F_c and coherent positions P_c. Solid lines show F_c and P_c calculated for a linear expansion of the box models for Fe, Cr, and Ni, as shown in Figure 1c. Short and long dashed lines indicate corresponding experimental results for the pristine and the electrolyte exposed film, respectively, with experimental error bars indicated. Within the limits of error, a common value of $x \approx 1.12$, marked by dotted lines, is in agreement with the data.

XSW spacing d_{ML}. Further increase in the width leads to an increase in both F_c and P_c. This behavior was discussed earlier briefly and is elaborated in more detail in Supporting Information. Thus, the whole film has expanded. Iron, being distributed over the whole film thickness (Figure 1c), shows the largest change in the coherent position.

The new metal distribution, modeled again by a square box profile, is shown in Figure 4b. Except for the overall increase in thickness, the distribution is rather similar to the intrinsic distribution shown in Figure 1c. The new square box profile of the distribution allows to reproduce F_c and P_c perfectly for Cr and Ni, but only with some minor deviation for Fe, which indicates that, not surprisingly, the box profile represents only a first-order approximation. The parameters P_c and F_c obtained by adjusting/fitting the box profile to best reproduce the data are shown in Table 1 and 2.

With the help of the experimental coherent fractions and based on the box model, the expansions e_F of the distribution of the three metals following hydrogen exposure can be calculated from the change in the widths ΔP (Table 2) of the intrinsic box profile, i.e., $e_F = [\Delta P(\text{hydrogen}) - \Delta P(\text{pristine})]/\Delta P(\text{pristine})$. Exploiting also the measured coherent positions, the expansion e_P is given by $e_P = 2\ \Delta P_c/\Delta P(\text{pristine})$, with $\Delta P_c = P_{c,H} - P_{c,P}$, where $P_{c,H}$ and $P_{c,P}$ are the metal coherent positions of the electrolyte exposed and the pristine film, respectively. Ideally, $e_F = e_P$, but as Table 2 shows, this is not the case, which is another indication of the limitations of the square box model. The scattering of the expansion coefficients is fairly large but they consistently point to a significant expansion of the film. If we assume the expansion being homogeneously the same for all three metals, it can be estimated from the average of the six e_F, e_P values as $(11.3 \pm 3)\%$.

The expansion can also be graphically modeled/simulated by assuming, in a first-order approximation, that the width of the pristine distribution of each of the three metals has expanded linearly by a factor x, i.e., the widths of the square boxes of the metals in the pristine film are increased by a factor x. Accordingly calculated coherent fractions F_c and positions P_c for each of the three metals are shown in Figure 4c as a function of expansion factor x. Assigning a common expansion factor to all three metals is (barely) possible, but within the limits or error, an acceptable agreement of calculated and measured coherent fractions and positions is achieved for $x \approx 1.2$ i.e., ≈12% expansion of the film, marked by the dotted lines Figure 4c.

Thickness increase due to metal adsorption from the electrolyte can be excluded based on X-ray fluorescence analysis and because of the ultrapure chemicals used. Swelling of the film by metal oxidation can also be excluded, as exposure to cathodic potential of −0.6 $V_{Ag/AgCl}$ leads to the opposite, i.e., metal oxide reduction, proven by XANES (Figure 3b).

The increase in film thickness is caused by hydrogen absorption. The cathodic current (Figure 3a) originates 1) from reduction of metal oxide and solved oxygen and 2) from hydrogen evolution (in part also causing metal oxide reduction[36]), as described e.g., by Babić and Metikoš-Huković[37] and Dafft et al.[38] Hydrogen evolution by electrochemical reduction of hydrated hydrogen ions follows the so-called Volmer reaction.[38,39] In near-neutral pH solution, as in this case, hydrogen evolution occurs predominantly via reduction of water molecules.[29] This produces in the first step surface-adsorbed atomic hydrogen. A part of the adsorbed hydrogen reacts to form molecular hydrogen via the Tafel or Heyrovsky reaction.[38] However, in a parallel process, atomic hydrogen is absorbed.[38,40,41]

It is well known that hydrogen absorption causes lattice expansion and eventually phase transformations of steel, leading to a significant volume increase.[13,30,42–44] However, because of competing processes mentioned earlier and to overcome strain energy, significant bulk absorption typically requires high cathodic current densities.[40,45,46] Bulk absorption of ≈25 at% needs a current density of at least 2 mA cm^{-2} in 0.5 M H_2SO_4, i.e., ≈30 times a higher current density than here (Figure 3a), and absorption of 15 at% hydrogen leads to a 3% volume

change.[40] By a simple linear extrapolation, the 11–12% volume change found here requires absorption of ≈60 at% hydrogen, i.e., 0.6 hydrogen per metal atom in the film. This points to an astonishing absorption efficiency. Of the total electron transfer of $2.4 \times 10^{17} e_0$ cm^{-2}, recorded during exposure, a significant amount (more than ≈10%) must have been invested in the production of H^+ of which then 2×10^{16} cm^{-2} subsequently was absorbed by the steel film (containing 3.3×10^{16} metal atoms per cm^2). Very significant hydrogen absorption into the film had occurred obviously at a rather mild cathodic potential and at more than an order of magnitude lower current density, compared with typical hydrogen loading of bulk steel.

The lattice expansion following hydrogen absorption causes significant compressive strain and the associated increasing elastic energy limits the amount of hydrogen that can be absorbed into bulk steel. Thus, decreasing the strain energy should allow increasing the amount of hydrogen absorbed, which has indeed been observed. Hydrogen absorption is enhanced when subjecting steel to tensile stress.[43,47,48] In this context, it is important to realize that the surface, or a thin film, can easily expand in one direction. Consequently, strain energy as well as the energy barrier for transition from elastic to plastic deformation such as buckling caused by hydrogen loading will be considerably lower than for the bulk process. Obviously dimensionality matters for the maximum uptake of hydrogen at given chemical potential (of hydrogen) because of the corresponding scaling of strain and deformation energy and the surface may be much more severely affected by the hydrogen exposure than bulk of the steel.

The here-observed hydrogen-induced expansion of ≈11% is by far too large to be accommodated by elastic deformation, whether in the bulk or thin film, and the swelling must be accompanied by plastic deformation.[46] This is consistent with reported hydrogen-induced embrittlement.[4,30,49] Severe local structural disruption of the protective passive layer induced by swelling is also a plausible explanation for the reported hydrogen-induced diminished resistance to pitting corrosion.[28]

4. Conclusions

In summary, an ≈4 nm-thick FeCrNi film with a metal composition close to SS 304 was used to study structural changes induced by electrolytic hydrogen charging at cathodic potential. Using a ML as a substrate, the XSW technique in combination with XANES allowed analyzing the distribution and oxidation state of Cr, Fe, and Ni depth-selectively. Approximating the distributions of the three metals in the film by simple square box profiles, the analysis revealed characteristic features of metal distribution. The 2 nm passive surface layer consists of oxidized Fe and Cr and is depleted of Ni. Structure and composition of the film appear to represent a useful substitute for the real surface region of SS.[8,12,23,33] Using such a thin film offers the advantage of obtaining exceedingly precise information on the surface compositional and structural changes using X-ray techniques such as XSW and XANES.

Exposure to 0.1 M KCl electrolyte for 10 min at $-0.6\,V_{Ag/AgCl}$ resulted in a cathodic charge transfer of $2.4 \times 10^{17} e_0$ cm^{-2}, leading to strong ≈11% swelling of the film. Fluorescence analysis proved that the amount of metal in the film had not changed and the expansion of the film is explained by hydrogen absorption, estimated to be about 60 at%. The data indicate that the expansion of the film is not homogeneous, which is not surprising, considering the inhomogeneous metal concentration and probably correspondingly inhomogeneous H absorption. Worthy of note, H exhibits high solubility in electrolytically charged Ni metal, leading to a hydride phase with 0.6 H per Ni.[50] Although the experimental conditions are not comparable, other reports seem to suggest that the solubility in Fe[51] and Cr[52] metal is much lower.

Compared with the electrolytically hydrogen charging of bulk steel, a much lower cathodic current density leads to the strong hydrogen uptake and volume expansion of the thin film, which can be understood as an effect of dimensionality. A 2D-like thin film (or surface layer) may expand in just one direction and the associated strain energy will be much lower than that required for expansion of the 3D bulk. It is noteworthy that swelling of 11% is not compatible with elastic strain and will cause disruption of the passivating layer, likely more or less pronounced locally. These findings should be seen in view of the decrease in the pitting corrosion resistance of steel surfaces,[28–30] reported as the result of hydrogen exposure.

5. Experimental Section

The used steel film was grown at room temperature on the B_4C surface of a Ru/B_4C ML with a *d*-spacing d_{ML} 3.91 nm (see Supporting Information) using direct current (DC) magnetron sputter deposition. Low-carbon austenitic SS 304, an alloy consisting ≈97% of Fe, Cr, and Ni,[53] was used as target material for the sputter process. X-ray fluorescence analysis of the steel film revealed the metal concentration ratios of Fe/Cr = 4.3 and Fe/Ni = 9.0.[34] This corresponded to Cr and Ni concentrations of 17% and 8%, respectively. Compared with the ranges of 18–20% and 8–12% for Cr and Ni, respectively; for SS304,[53] the film was found slightly low in nickel and chromium content. Determined by XRR measurements, the material thickness of the film on the ML was about 4 nm. The film thickness was chosen close to the *d*-spacing of the ML, allowing XSW measurements with a high sensitivity. Details on the growth and characterization using X-ray as well as electrochemical techniques are reported in a forthcoming communication article.[34]

Emission-mode XANES and XSW measurements were carried out on the P64 undulator beamline at PETRA-III, DESY, Hamburg, acquiring X-ray fluorescence with the help of an energy-dispersive solid-state detector.[54] XSW measurements were carried out above the Ni *K*-edge (8333 eV), scanning the energy E_γ across the first-order Bragg peak of the ML. The angle of incidence of the beam on the ML was adjusted, such that the reflectivity of first-order ML reflection was at maximum at 10 keV, i.e., in the middle of the 2 keV scan range. This corresponded to a grazing angle of incidence of ≈0.945°. *K*-edge XANES spectra of Cr, Fe, and Ni were also acquired under XSW conditions by simultaneously scanning angle and energy. As described, this allows acquiring XANES spectra with enhanced X-ray intensity in specific regions in the film.[35] In this way, chemical information on the metal oxidation states was obtained depth-selectively.

Supporting Information

Supporting Information is available from the Wiley Online Library or from the author.

Acknowledgements

The research leading to this publication was supported by the project CALIPSOplus under the grant agreement 730872 from the EU Framework Programme for Research and Innovation HORIZON 2020. A major part of the experimental work was carried out at beamline P64 at DESY, a member of the Helmholtz Association (HGF) supplemented by work at beamlines B18, B16, as well as the optics lab at DLS. The authors would like to thank Wolfgang Caliebe for help and advice during the experiments at P64. A.W. has received funding from the European Union's Horizon 2020 research and innovation program under the Marie Skłodowska-Curie grant agreement (GA) no 665593 awarded to the Science and Technology Facilities Council. V.S. acknowledges financial support by the Austrian Academy of Sciences via DOC fellowship and DG by DST/INSPIRE Fellowship/[IF160579], awarded by the Government of India Ministry of Science and Technology.

Conflict of Interest

The authors declare no conflict of interest.

Keywords

hydrogen loading, stainless steels, thin films, X-ray spectroscopy, X-ray standing waves

Received: January 27, 2020
Revised: March 18, 2020
Published online: April 2, 2020

[1] X. G. Zhang, *Uhlig's Corrosion Handbook*, Third Edition, (Ed: R. W. Revie), John Wiley & Sons, New York **2011**, pp. 123–143.
[2] C. Örnek, C. Leygraf, J. Pan, *NPJ Mater. Degrad.* **2019**, *3*, 8.
[3] M. Hampel, M. Schenderlein, C. Schary, M. Dimper, O. Ozcan, *Electrochem. Commun.* **2019**, *101*, 52.
[4] M. L. Holzworth, *Corrosion* **1969**, *25*, 107.
[5] M. Hatano, M. Fujinami, K. Arai, H. Fujii, M. Nagumo, *Acta Mater.* **2014**, *67*, 342.
[6] A. Atrens, Q. Liu, C. Tapia-Bastidas, E. Gray, B. Irwanto, J. Venezuela, Q. Liu, *Corros. Mater. Degrad.* **2018**, *1*, 3.
[7] G. Koch, *Woodhead Publishing Series In Energy*, Woodhead Publishing, Swaston, UK **2017**, pp. 3–30.
[8] C.-O. A. Olsson, D. Landolt, *Electrochim. Acta* **2003**, *48*, 1093.
[9] A. Kocijan, Č. Donik, M. Jenko, *Corros. Sci.* **2007**, *49*, 2083.
[10] R. Jiang, Y. Wang, X. Wen, C. Chen, J. Zhao, *Appl. Surf. Sci.* **2017**, *412*, 214.
[11] R. Wang, Y. Li, T. Xiao, L. Cong, Y. Ling, Z. Lu, C. Fukushima, I. Tsuchitori, M. Bazzaoui, *Sci. Rep.* **2019**, *9*, 13094.
[12] Y. Gui, Z. J. Zheng, Y. Gao, *Thin Solid Films* **2016**, *599*, 64.
[13] L. Q. Guo, S. X. Qin, B. J. Yang, D. Liang, L. J. Qiao, *Sci. Rep.* **2017**, *7*, 3317.
[14] M. P. Ryan, D. E. Williams, R. J. Chater, B. M. Hutton, D. S. McPhail, *Nature* **2002**, *415*, 770.
[15] V. Yakubov, M. Lin, A. A. Volinsky, L. Qiao, L. Guo, *NPJ Mater. Degrad.* **2018**, *2*, 39.
[16] P. Guo, E. Callagon La Plante, B. Wang, X. Chen, M. Balonis, M. Bauchy, G. Sant, *Sci. Rep.* **2018**, *8*, 7990.
[17] S. C. Hayden, C. Chisholm, R. O. Grudt, J. A. Aguiar, W. M. Mook, P. G. Kotula, T. S. Pilyugina, D. C. Bufford, K. Hattar, T. J. Kucharski, I. M. Taie, M. L. Ostraat, K. L. Jungjohann, *NPJ Mater. Degrad.* **2019**, *3*, 17.
[18] A. Bianconi, *Appl. Surf.* **1980**, *6*, 392.
[19] B. W. Batterman, *Phys. Rev.* **1964**, *133*, A759.
[20] *The X-Ray Standing Waves Technique: Principles And Applications* (Eds: J. Zegenhagen, A. Y. Kazimirov), World Scientific, Singapore **2013**.
[21] J. Zegenhagen, *Jpn. J. Appl. Phys.* **2019**, *58*, 110502.
[22] D. A. López, W. H. Schreiner, S. R. de Sánchez, S. N. Simison, *Appl. Surf. Sci.* **2003**, *207*, 69.
[23] P. Gümpel, A. Hörtnagl, *Mater. Corros.* **2016**, *6*, 607.
[24] A. Nazarov, F. Vucko, *Electrochim. Acta* **2016**, *216*, 130.
[25] L. Ma, F. Wiame, V. Maurice, P. Marcus, *NPJ Mater. Degrad.* **2019**, *3*, 29.
[26] C. Punckt, M. Bölscher, H. H. Rotermund, A. S. Mikhailov, L. Organ, N. Budiansky, J. R. Scully, J. L. Hudson, *Science* **2004**, *305*, 1133.
[27] W. Shi, S. Yang, J. Li, *Sci. Rep.* **2018**, *8*, 4830.
[28] S. Ningshen, U. Kamachi Mudali, G. Amarendra, P. Gopalan, R. K. Dayal, H. S. Khatak, *Corros. Sci.* **2006**, *48*, 1106.
[29] Y. F. Cheng, L. Niu, *Electrochem. Commun.* **2007**, *9*, 558.
[30] S. Thomas, N. Ott, R. F. Schaller, J. A. Yuwono, P. Volovitch, G. Sundararajan, N. V. Medhekar, K. Ogle, J. R. Scully, N. Birbilis, *Heliyon* **2016**, *2*, e00209.
[31] J. Zegenhagen, *Surf. Sci. Rep.* **1993**, *18*, 202.
[32] M. J. Bedzyk, J. A. Libera, *The X-Ray Standing Wave Technique – Principles And Applications* (Eds: J. Zegenhagen, A. Kazimirov)), World Scientific, Singapore **2013**, p. 122.
[33] R. P. Frankenthal, D. L. Malm, *J. Electrochem. Soc.* **1976**, *123*, 186.
[34] D. Garai, V. Solokha, A. Wilson, I. Carlomagno, A. Gupta, M. Gupta, V. R. Reddy, C. Meneghin, F. Carla, C. Morawe, J. Zegenhagen, Unpublished.
[35] A. Gupta, D. Kumar, C. Meneghini, J. Zegenhagen, *J. Appl. Phys.* **2007**, *101*, 09D117.
[36] H.-Y. Lin, Y.-W. Chen, C. Li, *Thermochim. Acta* **2003**, *400*, 61.
[37] R. Babić, M. Metikoš-Huković, *J. Appl. Electrochem.* **1993**, *23*, 352.
[38] E. G. Dafft, K. Bohnenkamp, H. J. Engell, *Corros. Sci.* **1979**, *19*, 591.
[39] Z. Li, C. Yang, G. Cui, S. Zhang, C. Zhang, *Anti Corros-Method M.* **2019**, *66*, 203.
[40] D. G. Ulmer, C. J. Altstetter, *Acta Metal. Mater.* **1993**, *41*, 2235.
[41] S. Thomas, G. Sundararajan, P. D. White, N. Birbilis, *Corrosion* **2017**, *73*, 426.
[42] R. N. Iyer, H. W. Pickering, M. Zamanzadeh, *Scripta Metallurgica* **1988**, *22*, 911.
[43] B. Ozdirik, T. Suter, U. Hans, T. Depover, K. Verbeken, P. Schmutz, L. P. H. Jeurgens, H. Terryn, I. De Graeve, *Corros. Sci.* **2019**, *155*, 55.
[44] L. Claeys, T. Depover, I. De Graeve, K. Verbeken, *Corrosion* **2019**, *75*, 880.
[45] A. Szummer, A. Janko, *Corrosion* **1979**, *35*, 461.
[46] A. P. Bentley, G. C. Smith, *Metall. Trans. A* **1986**, *17*, 1593.
[47] T. Zakroczymski, *Corrosion* **1985**, *41*, 485.
[48] Y. Huang, A. Nakajima, A. Nishikata, T. Tsuru, *ISIJ Int.* **2003**, *43*, 548.
[49] R. Scharf, A. Muhr, K. H. Stellnberger, J. Faderl, C. Holzer, G. Mori, *Mater. Corros.* **2017**, *68*, 95.
[50] E. O. Wollan, J. W. Cable, W. C. Koehler, *J. Phys. Chem. Solids* **1963**, *24*, 1141.
[51] W. Y. Choo, J. Y. Lee, C. G. Cho, S. H. Hwang, *J. Mater. Sci.* **1981**, *16*, 1285.
[52] D. Wallinder, G. Hultquist, B. Tveten, E. Hörnlund, *Corros. Sci.* **2001**, *43*, 1267.
[53] https://www.aksteel.com/sites/default/files/2018-11/304-304l-stainless.pdf.
[54] W. A. Caliebe, V. Murzin, A. Kalinko, M. Görlitz, *AIP Conf. Proc.* **2019**, *2054*, 060031.